Catalysis Today 163 (2011) 27–32

Contents lists available at ScienceDirect

Catalysis Today

journal homepage: www.elsevier.com/locate/cattod

# Combining confinement and NO calcination to arrive at highly dispersed supported nickel and cobalt oxide catalysts with a tunable particle size

Mariska Wolters, Lotte J.W. van Grotel, Tamara M. Eggenhuisen, Jelle R.A. Sietsma[1], Krijn P. de Jong, Petra E. de Jongh*

*Inorganic Chemistry and Catalysis, Debye Institute for NanoMaterials Science, Utrecht University, NL-3584 CA Utrecht, The Netherlands*

ARTICLE INFO

*Article history:*
Available online 25 March 2010

*Keywords:*
Impregnation
Cobalt
Nickel
Nanoparticles
Nitric oxide
Supported catalysts

ABSTRACT

Control over the size and size distribution of supported nanoparticles is key to their efficient use in catalysis. In the preparation of nanoparticles by impregnation using nitrate precursors, the support pore diameter can be used to influence the average crystallite size. However, the particle size distributions obtained via this method are generally broad and the dispersions relatively low. Higher dispersions and narrow particle size distributions are obtained via thermal decomposition of the metal nitrate precursor in 1% (v/v) NO in Ar instead of air. Here we will show that by combining the confinement effect of ordered mesoporous silica with a decomposition step of metal nitrates in NO, silica supported nickel and cobalt oxides with a tunable particle size (2–4 nm) can be obtained at high loadings (10–20 wt%).



## 1. Introduction

Supported metal (oxide) catalysts are essential for the production of fuels and chemicals as well as the reduction of environmental pollution. Nickel and cobalt based catalysts are frequently used as they find application in industrial processes such as the hydrogenation of edible oils, steam reforming, methanation and the Fischer–Tropsch synthesis [1,2]. Recently, it has also been shown that small supported $Co_3O_4$ particles are efficient catalysts for the photocatalytic oxidation of water [3]. The activity and selectivity of catalyst nanoparticles strongly depend on their physical properties, such as size, distribution and shape [4]. Especially control over the size and size distribution is a key to the efficient use of metal (oxide) nanoparticles [5–7]. In most catalytic reactions, the activity is proportional to the metal (oxide) surface area, thus favoring high surface to volume ratios. However, non-continuous trends are observed for nanoparticles smaller than 10 nm. An example is the dependence of the Fischer–Tropsch synthesis activity on the cobalt particle size, where a sharp optimum in activity was found for 6 nm Co particles [8,9]. Highly dispersed metals can be prepared by deposition from the vapor or liquid phase onto a support (e.g. $SiO_2$ or $Al_2O_3$) [10–12]. In the industry, supported metal (oxides) are most often prepared by impregnation of a support material with aqueous solutions containing metal precursors. Organic precursors yield high dispersions, however, due to limited solubility multiple impregnation steps are often required to achieve the desired metal loading [13]. Inorganic precursors such as nitrates, sulfates and chlorides generally have much higher solubility in water, which allows high loadings in a single impregnation step. Nitrate precursors, in contrast to sulfate and chloride precursors, yield pure metal oxides after heat treatment and are therefore mostly used. On the other hand, nitrate precursors have the major disadvantage that they typically yield poor dispersions due to agglomeration during drying and thermal treatment (calcination) [13,14]. Recently it was shown that replacement of the air calcination by a 1% (v/v) NO/He thermal treatment, prevents this agglomeration, resulting in highly dispersed supported cobalt and nickel oxides at high loadings [15,16]. The high dispersions were ascribed to the ability of NO to scavenge oxygen radicals which are produced during the decomposition of the nitrate, resulting in a moderated decomposition [16].

Although yielding a very high dispersion, control over the particle size still remains a challenge. In literature the pore structure of the support has been used to confine the crystal growth. Cobalt clusters and nanoparticles with different diameters have been prepared from nitrate precursors by variation of the pore diameter of MCM-41 [17,18], albeit at loadings below 5 wt%. Li et al. used higher loadings (15 wt% Co) for their studies on silicagel, SBA-15 and MCM-48, and confirmed that smaller pores resulted in a decrease in average particle diameter [19]. Similar observations were reported by Borg et al. on commercial alumina supports with

* Corresponding author at: Sorbonnelaan 16, 3584 CA Utrecht, The Netherlands. Tel.: +31 30 253 6766/7400; fax: +31 30 251 1027.
*E-mail address:* p.e.dejongh@uu.nl (P.E. de Jongh).
[1] Present address: Shell Global Solutions, NL-1030 BN Amsterdam, The Netherlands.

0920-5861/$ – see front matter © 2010 Elsevier B.V. All rights reserved.
doi:10.1016/j.cattod.2010.02.052

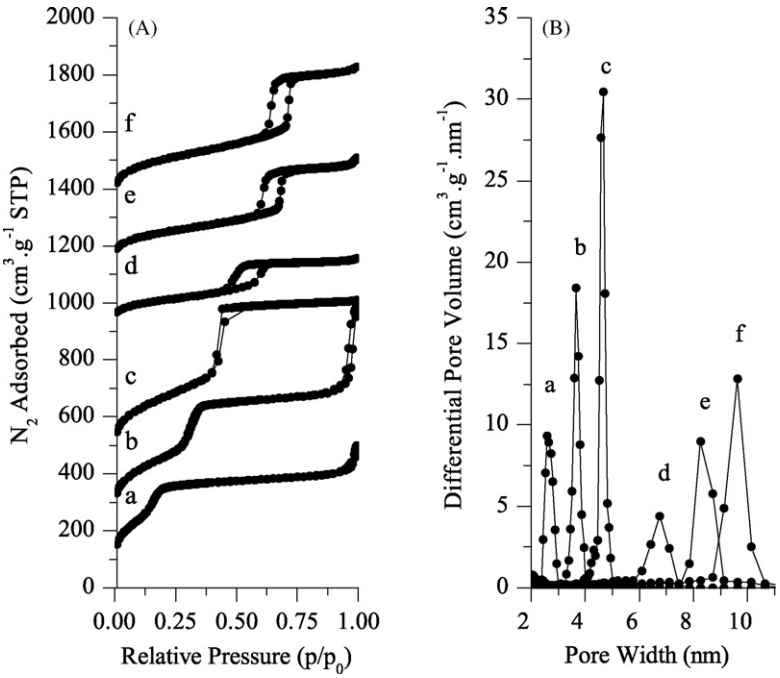


**Fig. 1.** $N_2$-physisorption isotherms (A) and differential pore size distributions (B) of pristine (a) MCM-2.5, (b) MCM-3.7, (c) MCM-4.6, (d) SBA-6.7, (e) SBA-8.3 and (f) SBA-9.6.

varying pore diameters [20]. From these reports it is clear that confinement by the pores is a promising approach to tune the particle size of supported metal oxides prepared by impregnation. However, the average crystallite size was usually larger than the support pore diameter, and the particle size larger than the crystallite size, which may be expected considering the tendency of cobalt oxide to agglomerate [20–22]. In addition to the reduced metal surface area caused by agglomeration, reduced accessibility and stability of the active sites due to plugging of the pores may deteriorate the catalyst performance.

In this contribution we have combined the use of ordered mesoporous supports with the moderated metal nitrate decomposition under NO to control the nickel and cobalt oxide particle size. We will show that this combination results in highly dispersed cobalt and nickel oxides with narrow particle size distributions. Furthermore, the average particle size can be tuned via the pore diameter of the support, and the crystallite size and particle size coincide.

## 2. Experimental

### 2.1. Sample preparation

SBA-15 was prepared according to literature [23]. Materials with different average pore diameters were obtained by aging at 80 °C (pore diameter (PD) = 9.7 nm), 60 °C (PD = 8.3) and 40 °C (PD = 6.7 nm). MCM-41 was synthesized according to the procedure reported by Cheng et al. [24]. Materials with three different pore diameters were synthesized by variation of the template; $C_{13}H_{30}NBr$ (PD = 2.5 nm), $C_{19}H_{42}NBr$ (PD = 3.7 nm) and $C_{17}H_{38}NBr$ (PD = 4.6 nm). The aging temperature was 100 °C for the first two templates and 150 °C for the latter. After synthesis the support materials are coded as follows: support name followed by the pore diameter, e.g. SBA-9.6.

Nickel loaded samples were prepared by impregnating to incipient wetness with 4.2 M aqueous nickel nitrate solution. After impregnation the sample was dried in stagnant air at 120 °C for 12 h. Calcination was performed at 350 °C in a flow of air or 1% (v/v) NO/Ar, using a heating rate of 5 °C/min and a dwell time of 2 h. Cobalt loaded samples were prepared similarly, by impregnating to incipient wetness with 3 M aqueous cobalt nitrate solution. After impregnation the cobalt sample was dried at 60 °C for 12 h in stagnant air, and calcined at 240 °C in a flow of air or 1% (v/v) NO/Ar, using a heating rate of 1 °C/min and a dwell time of 2 h. The metal loading was 13–22 wt% depending on the specific pore volume of the support.

Impregnated samples are labeled by the addition of the metal type (e.g. SBA-9.6-Ni) and heat treatment by addition of the gas atmosphere during calcination to the name (e.g. SBA-9.6-Ni-NO).

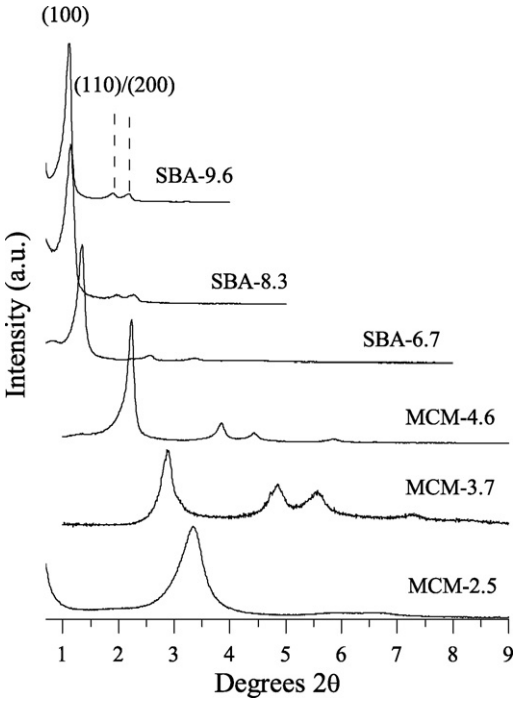


**Fig. 2.** Low-angle XRD patterns of the pristine MCM-41 and SBA-15 samples.

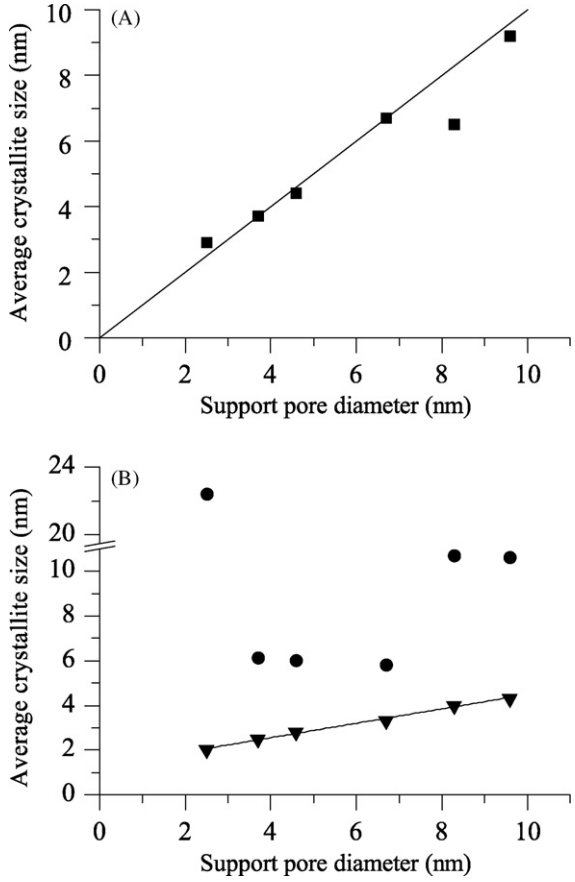


**Fig. 3.** Relation between the support diameter and (A) the average $Ni_3(NO_3)_2(OH)_4$ crystallite size obtained after impregnation and drying (■), (B) the average NiO crystallite size obtained after NO (▼) and air calcination (●).

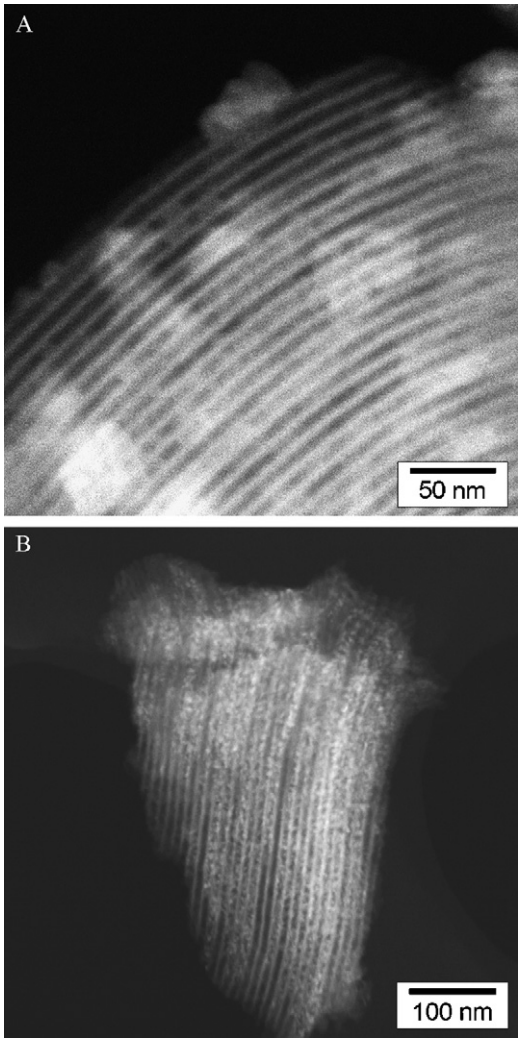


**Fig. 4.** HAADF-STEM image of SBA-9.6-Ni after calcination in air (A) and 1% (v/v) NO/Ar (B).

### 2.2. Characterization

Powder X-ray diffraction (XRD) patterns were obtained at room temperature from 10 to 80° 2$\theta$ with a Bruker-AXS D8 Advance X-ray Diffractometer setup using Co $K_{\alpha 12}$ radiation ($\lambda$ = 0.179 nm). The average $Ni_3(NO_3)_2(OH)_4$, NiO and $Co_3O_4$ crystallite size was calculated from the most intense lines at 14.9° (0 0 1), 50.8° (2 0 0) and 43.1° (3 1 1) 2$\theta$, respectively.

$N_2$-physisorption measurements were performed at −196 °C, using a Micromeretics Tristar 3000 apparatus. Prior to the measurement the samples were degassed in a flow of nitrogen at 300 °C for 12 h. Pore size distributions were derived from the adsorption branch of the isotherm, using non-local density functional theory (NL-DFT) [25]. The mesopore surface area was determined with the *t*-method [26], using the Harkins and Jura thickness equation [27], by subtracting the slope of the *t*-plot in the 1.00–1.40 nm thickness range from the 0.35–0.55 nm range.

Scanning transmission electron microscopy (STEM) and transmission electron microscopy (TEM) images were obtained on a Tecnai 20 apparatus, operated at 200 keV. High angle annular dark field (HAADF) images were typically taken at a camera length of 150 mm. The average NiO particle size on the external surface was determined by counting a total of 150 NiO particles on 5 different support particles.

**Table 1**
Overview $N_2$-physisorption results and unit cell sizes for the pristine supports.

| Sample | $d_{pore}$[a] (nm) | $a_o$[b] (nm) | $S_{meso}$[c] ($m^2\ g^{-1}$) | Porosity ($cm^3\ g^{-1}$) | | |
|---|---|---|---|---|---|---|
| | | | | $V_{tot}$[d] | $V_{meso}$[e] | $V_{micro}$[f] |
| MC-2.5 | 2.5 | 3.6 | 1188 | 0.65 | 0.60 | 0 |
| MC-3.7 | 3.7 | 4.1 | 888 | 0.80 | 0.71 | 0 |
| MC-4.6 | 4.6 | 5.3 | 914 | 0.94 | 0.92 | 0 |
| SBA-6.7 | 6.7 | 8.8 | 264 | 0.38 | 0.37 | 0.05 |
| SBA-8.3 | 8.3 | 10.3 | 338 | 0.59 | 0.57 | 0.05 |
| SBA-9.6 | 9.6 | 11.0 | 450 | 0.79 | 0.77 | 0.08 |

[a] Pore diameter determined using NL-DFT.
[b] Unit cell size determined from XRD ($a_o = 2 \times d(100)/\sqrt{3}$).
[c] Mesopore surface area determined using *t*-method.
[d] Total pore volume based on amount $N_2$ adsorbed at $p/p_0 = 0.95$.
[e] Mesopore volume determined using NL-DFT.
[f] Micropore volume determined using *t*-method.

## 3. Results

### 3.1. Support characterization

MCM-41 and SBA-15 with different mesopore diameters were prepared by variation of the template and synthesis temperature. Characterization of these materials by $N_2$-physisorption (Fig. 1) showed adsorption isotherms of the IV type, as expected for MCM-41 and SBA-15 materials. The textural properties derived from the measurements are given in Table 1. SBA-15, in contrast to

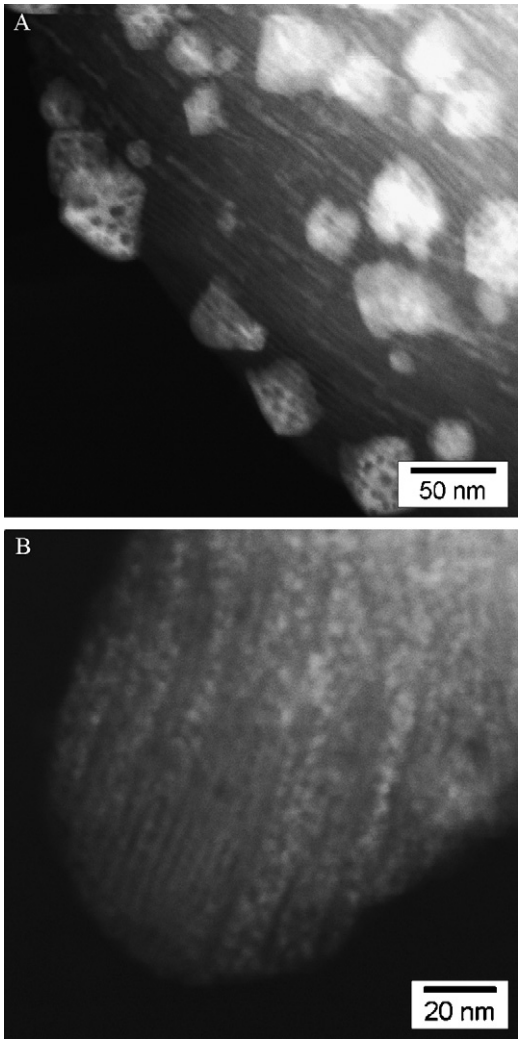


**Fig. 5.** HAADF-STEM image of SBA-4.6-Ni after calcination in air (A) and 1% (v/v) NO/Ar (B).

MCM-41, shows a clear H1 type hysteresis loop and a high onset at low $p/p_0$ values originating from the intra wall micro porosity. The steep increase in adsorption at high $p/p_0$ values in the case of MCM-3.7 indicates the presence of macro pores which could have been caused by aggregation of the relatively small support particles, as observed with TEM (data not shown). The pore size distributions in Fig. 1 show that all materials had uniform pore diameters, which ranged between 2.5 and 9.6 nm. The low-angle X-ray diffraction profiles of SBA-15 and MCM-41 showed reflections in the $2\theta$ range of 1–8° (Fig. 2) which could be indexed as the (1 0 0), (1 1 0) and (2 0 0) lattices of a unit cell with hexagonal symmetry [23]. The presence of higher order diffractions indicates uniformly ordered pore structures were obtained in all cases, with the exception of MCM-2.5. The decreasing unit cell size going from SBA-9.6 to MCM-2.5 is evident from the shift of the diffractions to higher $2\theta$ values, in agreement with the decreasing pore size (Table 1). The relatively larger shift in unit cell size between the SBA-6.7 and MCM-4.6 results from the thinner pore walls in MCM-41 [23].

### 3.2. Nickel oxide

First, the support materials were impregnated with an aqueous nickel nitrate solution, followed by drying at 120 °C. The resulting dried impregnate showed diffraction lines corresponding to

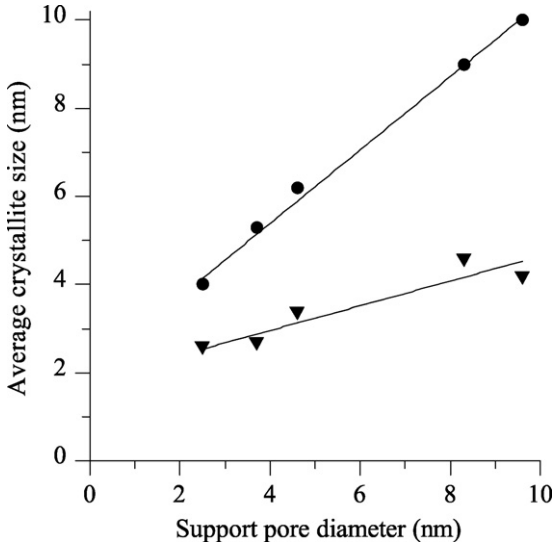


**Fig. 6.** Relation between the support diameter and the average $Co_3O_4$ crystallite size obtained after NO (▼) and air calcination (●).

a nickel hydroxynitrate phase with composition $Ni_3(NO_3)_2(OH)_4$ [28,29]. $Ni_3(NO_3)_2(OH)_4$ belongs to the family of double layered hydroxides (DLHs) and has a hexagonal unit cell with parameters $a = 3.13$ Å and $c = 6.89$ Å. Formation of $Ni_3(NO_3)_2(OH)_4$ during heating of nickel nitrate hexahydrate at 100–210 °C has been reported previously and is proposed to occur via the following decomposition reaction [29–32]:

$$3[Ni(OH_2)_6](NO_3)_2(aq) \rightarrow Ni_3(NO_3)_2(OH)_4(s) + 4HNO_3(g) + 14H_2O(g) \quad (1)$$

Characterization of the samples after drying was facilitated by presence of the $Ni_3(NO_3)_2(OH)_4$ crystallites, which could be detected by XRD. The clear peak broadening of the diffraction lines (supporting information, Fig. S-1) allowed calculation of the average crystallite size in the different samples. DLHs generally exhibit strong diffraction lines in the stacking direction, whereas the in-plane crystallization is generally poor. Consequently, only reliable calculations for the (0 0 1) diffraction line could be performed. In Fig. 3A the derived crystallite sizes are plotted as a function of the pore diameter. The clear one-to-one relation indicates that growth of the $Ni_3(NO_3)_2(OH)_4$ phase was confined by the pore walls. Indeed with TEM we observed no crystallites on the external surface of the material, indicating the phase was retained inside the pores during drying as we reported earlier [29].

Upon thermal treatment at 350 °C the nickelhydroxide nitrate phase is decomposed into nickel oxide. Topotactic conversion would result in a 30% shrinkage of the crystallite size, due to mass loss and density increase. However, the average NiO crystallite size after air thermal treatment was in all cases (with the exception of SBA-6.7-Ni) larger than the initial $Ni_3(NO_3)_2(OH)_4$ crystallite size (Fig. 3B, curve ●). This indicated that not only agglomeration had taken place, but also suggested that either transport to the external surface of the support particles had occurred, or that the pore structure had been destroyed by the crystallization process. Combined evidence from low-angle XRD, $N_2$-physisorption and STEM indicated that the pore structure had been retained during calcination. Therefore, the large crystallite size can be ascribed to transport of the nickel nitrate phase to the external surface. Figs. 4A and 5A show STEM images of SBA-9.6-Ni-air and SBA-4.6-Ni-air, which were representative for all samples. Part of the nickel oxide phase is retained inside the pores, exclusively forming rod like particles with a diameter equal to the pore diameter, further referred to as

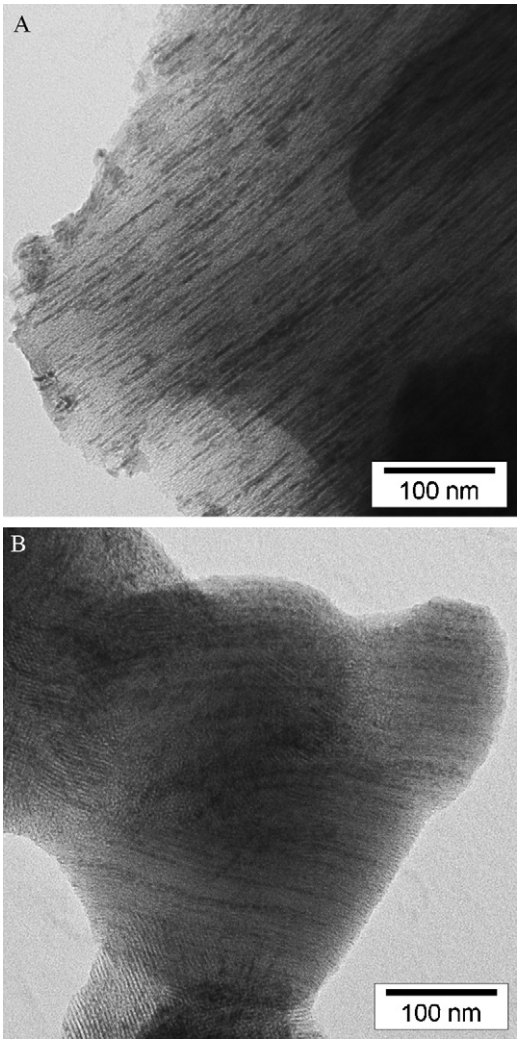


**Fig. 7.** TEM image of MCM-4.6-Co after calcination in air (A) and 1% (v/v) NO/Ar (B).

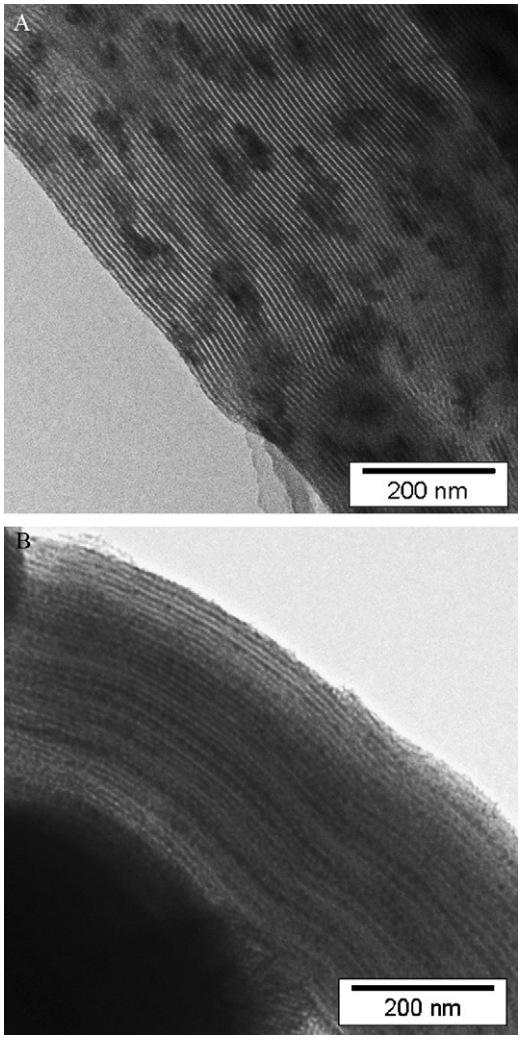


**Fig. 8.** TEM image of SBA-9.6-Co after calcination in air (A) and 1% (v/v) NO/Ar (B).

plugs. The remaining part is located on the external surface, forming 20–60 nm particles. However, with XRD no crystal domains of this size are detected, which suggests that the larger particles consist of multiple crystal domains. This is confirmed by the mesoporosity of the large NiO particles that is clearly observed in Fig. 5A. The large average crystallite size derived for MCM-2.5-Ni-air is at first surprising. This cannot be attributed to larger particles on the external surface as the number average, determined from STEM, was around 25 nm for all three MCM-41 samples. The most likely explanation is that the crystal domains inside the smallest pores are so small that they cannot reliably be detected with XRD. For the somewhat larger pores of MCM-3.7, a clear bimodal distribution is observed in the XRD (supporting information, Fig. S-2), where the sharp peak and the very broad feature can be ascribed to large crystals on the external surface and very small crystallites inside the pores. Therefore, the crystallites inside the even smaller MCM-2.5 pores are likely undetectable. Consequently, the volume average in this sample will mostly be determined by the particles on the external surface.

Fig. 3B (curve ▼) shows that NO calcination in all cases yields much smaller crystallites than air calcination (diffraction patterns shown in supporting information, Fig. S-3). STEM images of SBA-9.6-Ni-NO and SBA-4.6-Ni-NO (Figs. 4B and 5B) show that virtually all NiO particles are indeed located inside the pores and no plugs were formed. The retention of the phase in the pores, and the fact that the particle size is close to the crystallite size, explains the good correlation between the support pore diameter and the crystallite size shown in Fig. 3. It must be noted that the average NiO crystallite size in the larger pore samples is significantly smaller than expected from topotactic conversion. This can be attributed to fragmentation of the $Ni_3(NO_3)_2(OH)_4$ particles upon decomposition. For the MCM-41 materials the crystallite size is closer to the value expected from topotactic conversion. The difference could be explained using a similar argument as for the air calcination, that the crystallites inside the smallest pores are not detected.

### 3.3. Cobalt oxide

To prevent decomposition of cobalt nitrate to $Co_3O_4$ prior to the calcination, the drying temperature was lowered to 60 °C. Consequently the dried samples did not exhibit any diffraction lines.

XRD after air and NO calcination of the different cobalt nitrate impregnated supports resulted in broad peaks corresponding to $Co_3O_4$. As for the nickel samples the peak broadening was used to calculate the average crystallite size, and plotted against the pore diameter (Fig. 6). Here, also the air calcination (curve ●) of the cobalt samples yielded a clear relation between the average crystallite size and the pore diameter. However, the observed average crystallite size was still larger than the pore diameter. Closer investigation of MCM-4.6-Co-air and SBA-9.6-Co-air with TEM (Figs. 7A and 8A) revealed that again two types of particles

are present; large particles (6–20 nm) on the external surface and plugs inside the pores. In general less transport of metal oxide to the external surface is observed compared to nickel. Remarkably, for the SBA-15-Co samples the plugs appeared to be arranged into specific patches in the particle, whereas in the case of MCM-41 more isolated plugs were found. The difference between the two supports could originate from the difference in pore structure. SBA-15, unlike MCM-41, has microporous walls, and the apparent agglomeration suggests that transport of cobalt nitrate between adjacent pores has occurred. This phenomenon of clustering of $Co_3O_4$ crystallites has been observed before by others both with SBA-15 supports [3,21] and $\gamma$-$Al_2O_3$ [20,22].

The transport of cobalt nitrate species is dependent on the gas atmosphere, as is apparent from the results after NO calcination. Fig. 6, curve ▼ shows the average $Co_3O_4$ crystallite size after NO calcination as a function of the pore diameter. As for the nickel samples the size of the $Co_3O_4$ crystallites was related to the pore diameter, and were much smaller than for the air calcined samples. TEM images of MCM-4.6-Co-NO and SBA-9.6-Co-NO are depicted in Figs. 7B and 8B, respectively. Samples calcined in NO show pores filled with small particles as well as empty pores (Figs. 7B and 8B), which we previously ascribed to redistribution during drying rather than agglomeration during calcination [29,33]. However, plugs of cobalt oxide and agglomeration to specific patches in the SBA-15 particles were no longer observed, indicating that an improved distribution over the support particle was obtained.

## 4. Conclusions

We have shown that the average NiO and $Co_3O_4$ crystallite size can be tuned by variation of the support pore diameter. Essential to obtain highly dispersed particles with narrow particle size distributions from supported metal nitrates was the presence of nitric oxide during thermal decomposition of the precursor. Although the average $Co_3O_4$ and NiO crystallite sizes obtained by conventional thermal treatment in air were influenced by the pore size, particles typically consisted of agglomerates (2–60 nm) of crystallites, that beared only a rather poor correlation to the pore diameter. NO calcination, on the other hand, yielded high metal oxide dispersions and narrow particle size distributions that were well in agreement with the average crystallite size. Control over the particle size and distribution over the support is an essential factor to the activity and stability of supported catalysts. In this contribution nickel and cobalt oxide on ordered mesoporous silica were investigated as a case study, but it is anticipated that similar results will be obtained for other metals, such as copper, or more conventional supports such as silica gel.

## Acknowledgements

The authors kindly thank Hans Meeldijk and Cor van der Spek for the STEM and TEM analysis. Johnson Matthey Catalysts is acknowledged for the financial support and, especially Steve Pollington and John Casci for their scientific contributions to this work.

## Appendix A. Supplementary data

Supplementary data associated with this article can be found, in the online version, at doi:10.1016/j.cattod.2010.02.052.

## References

[1] M.W. Balakos, E.E. Hernandez, Catal. Today 35 (1997) 415.
[2] I. Chorkendorff, H. Niemantsverdriet, Concepts of Modern Catalysis and Kinetics, Wiley-VCH, Weinheim, 2007.
[3] F. Jiao, H. Frei, Angew. Chem. Int. Ed. 48 (2009) 1841.
[4] A.T. Bell, Science 299 (2003) 1688.
[5] M. Che, C.O. Bennett, Adv. Catal. 36 (1989) 55.
[6] G.A. Somorjai, J.Y. Park, Top. Catal. 49 (2008) 126.
[7] R.A. van Santen, Acc. Chem. Res. 42 (2009) 57.
[8] G.L. Bezemer, J.H. Bitter, H. Kuipers, H. Oosterbeek, J.E. Holewijn, X.D. Xu, F. Kapteijn, A.J. van Dillen, K.P. de Jong, J. Am. Chem. Soc. 128 (2006) 3956.
[9] J.P. den Breejen, P.B. Radstake, G.L. Bezemer, J.H. Bitter, V. Froseth, A. Holmen, K.P. de Jong, J. Am. Chem. Soc. 131 (2009) 7197.
[10] K.P. de Jong, Curr. Opin. Solid State Mater. Sci. 4 (1999) 55.
[11] K. Bourikas, C. Kordulis, A. Lycourghiotis, Catal. Rev. Sci. Eng. 48 (2006) 363.
[12] M.K. van der Lee, A.J. van Dillen, J.H. Bitter, K.P. de Jong, J. Am. Chem. Soc. 127 (2005) 13573.
[13] A.J. van Dillen, R.J.A.M. Terörde, D.J. Lensveld, J.W. Geus, K.P. de Jong, J. Catal. 216 (2003) 257.
[14] J. van de Loosdrecht, S. Barradas, E.A. Caricato, N.G. Ngwenya, P.S. Nkwanyana, M.A.S. Rawat, B.H. Sigwebela, P.J. van Berge, J.L. Visagie, Top. Catal. 26 (2003) 121.
[15] J.R.A. Sietsma, J.D. Meeldijk, J.P. den Breejen, M. Versluijs-Helder, A.J. van Dillen, P.E. de Jongh, K.P. de Jong, Angew. Chem. Int. Ed. 46 (2007) 4547.
[16] J.R.A. Sietsma, H. Friedrich, A. Broersma, M. Versluijs-Helder, A.J. van Dillen, P.E. de Jongh, K.P. de Jong, J. Catal. 260 (2008) 227.
[17] A.Y. Khodakov, A. Griboval-Constant, R. Bechara, F. Villain, J. Phys. Chem. B 105 (2001) 9805.
[18] A. Jentys, N.H. Pham, H. Vinek, M. Englisch, J.A. Lercher, Catal. Today 39 (1998) 311.
[19] H.L. Li, J.L. Li, H.K. Ni, D.C. Song, Catal. Lett. 110 (2006) 71.
[20] Ø. Borg, J.C. Walmsley, R. Dehghan, B.S. Tanem, E.A. Blekkan, S. Eri, E. Rytter, A. Holmen, Catal. Lett. 126 (2008) 224.
[21] J. van der Meer, I. Bardez, F. Bart, P.A. Albouy, G. Wallez, A. Davidson, Micropor. Mesopor. Mater. 118 (2009) 183.
[22] Ø. Borg, P.D.C. Dietzel, A.I. Spjelkavik, E.Z. Tveten, J.C. Walmsley, S. Diplas, S. Eri, A. Holmen, E. Rytter, J. Catal. 259 (2008) 161.
[23] D. Zhao, J. Feng, Q. Huo, N. Melosh, G.H. Fredrickson, B.F. Chmelka, G.D. Stucky, Science 279 (1998) 548.
[24] C. Cheng, D.H. Park, J. Klinowski, J. Chem. Soc. Faraday Trans. 93 (1997) 193.
[25] M. Jaroniec, M. Kruk, J.P. Olivier, S. Koch, Stud. Surf. Sci. Catal. 128 (2000) 71.
[26] B.C. Lippens, J.H. de Boer, J. Catal. 4 (1965) 319.
[27] W.D. Harkins, G. Jura, J. Am. Chem. Soc. 66 (1944) 1366.
[28] P. Gallezot, M. Prettre, Bull. Soc. Chim. Fr. 2 (1968) 407.
[29] J.R.A. Sietsma, J.D. Meeldijk, M. Versluijs-Helder, A. Broersma, A.J. van Dillen, P.E. de Jongh, K.P. de Jong, Chem. Mater. 20 (2008) 2921.
[30] K. Petrov, N. Zotov, E. Mirtcheva, O. Garciamartinez, R.M. Rojas, J. Mater. Chem. 4 (1994) 611.
[31] W. Brockner, C. Ehrhardt, M. Gjikaj, Thermochim. Acta 456 (2007) 64.
[32] J. Estelle, P. Salagre, Y. Cesteros, M. Serra, F. Medina, J.E. Sueiras, Solid State Ionics 156 (2003) 233.
[33] H. Friedrich, J.R.A. Sietsma, P.E. de Jongh, A.J. Verkley, K.P. de Jong, J. Am. Chem. Soc. 129 (2007) 10249.